Reaction Chemistry & Engineering

ROYAL SOCIETY OF CHEMISTRY

PAPER

View Article Online
View Journal

Check for updates

Cite this: DOI: 10.1039/d5re00397k

Facile room-temperature synthesis of hydroxysulfides for efficient oxygen evolution reaction

Pei-Wei Zhong,†[a] Hong-Xiao Yang,†[a] Wenkang Xu,[a] Zhiyang Yu,[a] Bei Li,[a] Yuguang Jin,[b] Hongjuan Wang,[a] Yonghai Cao,[a] Hao-Fan Wang,*[a] Yanhui Yang[c] and Hao Yu*[a]

Transition metal layered double hydroxides (LDHs) are among the most promising oxygen evolution reaction (OER) catalysts due to their abundant active sites and tunable metal composition. However, modulating metal species alone often fails to achieve optimal electronic structure. To address this, anionic regulation, such as sulfur incorporation, has been proposed as an effective strategy to further optimize the local electronic environment and enhance the OER performance. Despite this, conventional sulfurization approaches typically require harsh conditions, leading to phase transformation, lattice damage, and uneven sulfur distribution, thereby reducing structural integrity and catalytic activity. Herein, we develop a room-temperature sulfur doping strategy to introduce S^{2-} into nickel–iron-based LDH grown on nickel foam (NiFe-LDH/NF), yielding a hydroxysulfide catalyst (S-NiFe-LDH/NF) while retaining the original structure of LDH. This mild, energy-saving method enables uniform sulfur incorporation and effectively modulates the electronic states of metal sites. Importantly, the introduced sulfur ions induce enhanced surface reconstruction of the NiFe-LDH nanosheets under operating conditions, exposing more active sites and improving OER kinetics. The resulting S-NiFe-LDH/NF catalyst exhibits outstanding OER electrocatalytic performance, delivering a low overpotential of 235 mV at 200 mA cm^{-2} and a small Tafel slope of 45.3 mV dec^{-1} in 1.0 M KOH, significantly outperforming the pristine NiFe-LDH/NF and commercial RuO_2. Moreover, it demonstrates excellent long-term durability, maintaining over 90% of its initial current after 100 hours of continuous operation. This work presents a scalable structure-preserving strategy for sulfur doping in LDH-based electrocatalysts, offering a promising approach to design high-performance OER catalysts for sustainable hydrogen production *via* water electrolysis.

Received 7th September 2025,
Accepted 2nd January 2026

DOI: 10.1039/d5re00397k

rsc.li/reaction-engineering

Published on 21 January 2026. Downloaded by RSC Internal on 1/28/2026 11:03:34 AM.

1. Introduction

With the global shift toward clean energy and carbon neutrality, water electrolysis is gaining significant attention as a sustainable and eco-friendly hydrogen production technology.[1–4] Nevertheless, the anodic oxygen evolution reaction (OER), which entails a complex four-electron transfer process, remains sluggish due to substantial kinetic barriers, thus constituting a major bottleneck that hampers overall system efficiency.[5–11]

Among various electrocatalyst candidates, transition metal layered double hydroxides (LDHs) have emerged as promising materials, attributed to their compositional tunability and the abundance of catalytically active metal sites.[12–15] However, intrinsic limitations—such as poor charge-transfer kinetics, insufficient modulation of the electronic configuration at metal centres, and challenges in constructing well-defined two-dimensional architectures—continue to hinder their catalytic performance.[16–20] Therefore, developing effective strategies to tailor the electronic structure of LDHs has become a key objective in the design of high-performance OER electrocatalysts.

Sulfur doping has emerged as an effective strategy to modulate the electronic environment of metal centres, facilitating the adsorption and transformation of reaction intermediates and promoting the formation of highly active hydroxysulfide surface species.[7,21–23] In 2025, Roy *et al.*[24] developed a sulfur-doped $S_{8.3}$CoV-LDH catalyst that achieved a low OER overpotential of 250 mV at a current

[a] *School of Chemistry and Chemical Engineering, South China University of Technology, Guangzhou 510641, Guangdong, China. E-mail: whf@scut.edu.cn, yuhao@scut.edu.cn*
[b] *Ordos Laboratory, Ordos, Inner Mongolia 017010, China*
[c] *School of Chemistry and Molecular Engineering, Jiangsu National Synergetic Innovation Centre for Advanced Materials, Nanjing Tech University, Nanjing 211816, China*
† These authors contributed equally to this work.

Published on 21 January 2026. Downloaded by RSC Internal on 1/28/2026 11:03:34 AM.

density of 50 mA cm^{-2} under alkaline conditions, along with a Faradaic efficiency of 96%. Studies revealed that sulfur doping induces modulation of the metal valence states and structural optimization, significantly reduces the desorption energy barrier of *OOH, and enhances electrical conductivity and reaction kinetics, thereby effectively improving both the activity and stability of the OER process.

While these results underscore the great potential of sulfur doping in enhancing OER activity, its practical application remains hindered by significant challenges in synthesis. Conventional sulfurization techniques typically require high-temperature or reductive conditions to introduce sulfur anions into the precursor. Such harsh treatments often cause structural collapse, lattice distortion, or inhomogeneous sulfur distribution, which is particularly detrimental to structurally fragile two-dimensional LDHs. High temperatures may induce phase separation and structural degradation, leading to a drastic decrease in surface area and active site density, ultimately reducing catalytic stability and durability. In addition, the construction of NiFe-LDH precursors often relies on hydrothermal methods or alkaline co-precipitation, posing significant obstacles to achieving uniform morphology and consistent catalytic performance.[24–28]

To address these challenges, we propose a fully room-temperature synthetic route that integrates the room-temperature construction of the NiFe-LDH precursor with the subsequent sulfur doping step. The LDH nanosheet framework is formed by immersing pre-treated nickel foam into an aqueous $Fe(NO_3)_3$ solution under ambient conditions. This mild precursor synthesis avoids hydrothermal or alkaline co-precipitation routes, thereby ensuring structural uniformity, minimising impurity introduction, and preserving the two-dimensional layered morphology from the outset. Subsequently, sulfur doping is achieved by soaking the NiFe-LDH/NF in a concentrated Na_2S solution, wherein the exchangeable hydroxyl groups within the LDH lattice serve as entry points for sulfide ions. This post-synthetic treatment allows for uniform and deep sulfur incorporation without resorting to high-temperature or reductive conditions, thereby preventing structural degradation and phase separation while maintaining compositional homogeneity. Remarkably, this sulfur doping process under ambient conditions significantly promotes the electrochemical surface reconstruction of NiFe-LDH nanosheets, leading to enhanced exposure of active sites and accelerated OER kinetics.[29–33] The resulting S-NiFe-LDH/NF catalyst exhibits outstanding performance in 1.0 M KOH, requiring only 235 mV overpotential to reach 200 mA cm^{-2}, with a low Tafel slope of 45.3 mV dec^{-1}, greatly surpassing the undoped counterpart and commercial RuO_2. Furthermore, the catalyst demonstrates excellent long-term durability, retaining over 90% of its initial current density after 100 hours of continuous electrolysis. This work presents a fully ambient-temperature, scalable, and structure-preserving synthetic strategy encompassing both LDH construction and sulfur doping, providing a practical route to tailor the surface chemistry of LDH-based catalysts. The findings contribute valuable insights into the rational design of durable and efficient OER electrocatalysts and offer promising prospects for advancing sustainable hydrogen production and renewable energy technologies.[34–37]

2. Experimental section

2.1. Synthesis of the NiFe-LDH/NF electrode

A 1 × 1 cm^2 nickel foam (NF) substrate was sequentially immersed in acetone and 3 M hydrochloric acid solutions, followed by ultrasonic cleaning for 20 minutes in each to remove surface organic contaminants and oxide layers. After an initial rinse with deionized water, the substrate was transferred to anhydrous ethanol for a second ultrasonic treatment of equal duration. It was then dried overnight in a vacuum oven at 60 °C. The pretreated nickel foam was fully immersed in 40 mL of a 50 mM iron nitrate solution and maintained at room temperature for 4 hours. Afterward, it was removed, thoroughly rinsed with deionized water, and freeze-dried at −50 °C for 12 hours to obtain the final NiFe-LDH/NF product.

2.2. Synthesis of the S-NiFe-LDH/NF electrode

The 1 cm^2 NiFe-LDH/NF sample was fully immersed in 20 mL of 2 M sodium sulfide aqueous solution and subjected to a sulfidation reaction at room temperature for 14 hours. After thorough rinsing with deionized water, the sample was dried using a freeze-dryer at −50 °C for 12 hours, yielding the final target OER catalyst, S-NiFe-LDH/NF.

2.3. Electrochemical measurements and calculations

All electrochemical tests were conducted in 1.0 M KOH saturated with high-purity argon at room temperature using a standard three-electrode setup. Pre-measurement procedures are detailed in text S4. After measurements, all potentials were converted to the reversible hydrogen electrode (RHE) scale using the equation $E_{RHE} = E_{Hg/HgO} + E_{CAL}$, ($E_{RHE}$: electrode potential *versus* the reversible hydrogen electrode; $E_{Hg/HgO}$: electrode potential *versus* the Hg/HgO reference electrode; E_{CAL}: the calibration value of the Hg/HgO electrode *versus* the reversible hydrogen electrode). Linear sweep voltammetry (LSV) was performed at a scan rate of 5 mV s^{-1} to evaluate the OER activity. The overpotentials were reported after automatic iR compensation, which was applied at a 95% level by the electrochemical workstation based on the solution resistance (R_s) measured by EIS at 1.5 V *vs.* RHE prior to each test. The relationship between the overpotential (η) and current density (j) was analysed using the Tafel equation: $\eta = a + b\log j$, where b is the Tafel slope. EIS spectra were collected over the frequency range from 100 kHz to 0.01 Hz with a sinusoidal amplitude of 5 mV to

This journal is © The Royal Society of Chemistry 2026

Published on 21 January 2026. Downloaded by RSC Internal on 1/28/2026 11:03:34 AM.

determine the charge transfer resistance and solution resistance. Accelerated durability tests (ADT) were performed by continuous cyclic voltammetry (CV) within a potential window of 0–0.4 V (*vs.* RHE) at a scan rate of 100 mV s^{-1}. Long-term catalytic stability was evaluated *via* chronoamperometry (CA) or chronopotentiometry (CP) at a fixed potential or current density, respectively. To estimate the electrochemical surface area (ECSA), the double-layer capacitance (C_{dl}) was extracted from CV curves recorded in the non-faradaic potential window at scan rates ranging from 10 to 100 mV s^{-1}. The charging current (i_{dl}) was calculated as $i_{dl} = 0.5\ (i_{anode} - i_{cathode})$, and C_{dl} was determined as the slope of i_{dl} *versus* scan rate. The ECSA was calculated using the equation: ECSA = C_{dl}/C_s, assuming a specific capacitance (C_s) of 0.04 mF cm^{-2} for a smooth surface.

3. Results and discussion

3.1. Material characterization

The hydroxysulfide catalyst (S-NiFe-LDH/NF) was obtained entirely under room-temperature conditions, including both the LDH growth and the subsequent anion exchange process (Scheme 1). Photographs of the as-prepared NiFe-LDH/NF and S-NiFe-LDH/NF are shown in Fig. S1.

Due to the hydrolysis of Fe^{3+}, the pH of a 0.2 M $Fe(NO_3)_3$ solution is only 1.2.[38] When nickel foam is immersed in this acidic solution, nitrate ions and ferric ions act as oxidants that convert surface metallic nickel into Ni^{2+}. This process consumes protons at the interface and modulates the local pH, enabling the co-precipitation of Ni^{2+} and Fe^{3+} into NiFe-LDH/NF.[39,40] The detailed synthesis mechanism is provided in the SI. The subsequent sulfurization is achieved by immersing NiFe-LDH/NF in an aqueous solution of sodium sulfide. Due to the significantly lower solubility of metal sulfides compared to their corresponding hydroxides, sulfide ions in the solution gradually replace hydroxide ions in the solid phase based on the principle of solubility equilibrium. Taking $Ni(OH)_2$ as an example, at 25 °C, the solubility product (K_{sp}) of $Ni(OH)_2$ is 5.0×10^{-16}, while that of NiS is 1.0×10^{-21}. The dissolution equilibrium equation for NiS and $Ni(OH)_2$ is as follows:

$$NiS(s) + H_2O(l) \leftrightarrow Ni^{2+}(aq) + HS^-(aq) + OH^-(aq) \quad (3\text{-}1)$$

$$Ni(OH)_2(s) \leftrightarrow Ni^{2+}(aq) + 2OH^-(aq) \quad (3\text{-}2)$$

$$a_{Ni^{2+}} \times a_{OH^-}^2 = 5.0 \times 10^{-16} \quad (3\text{-}3)$$

$$a_{Ni^{2+}} \times a_{HS^-} \times a_{OH^-} = 1.0 \times 10^{-21} \quad (3\text{-}4)$$

When $Ni(OH)_2$ is placed in a 2.0 M sodium sulfide (Na_2S) solution, the ionic concentrations in the solution must simultaneously satisfy two specific equilibrium equations (eqn (3-3) and (3-4)). In the sodium sulfide solution, it is reasonable to assume that S^{2-} is almost completely hydrolyzed into HS^- and OH^-. Under this assumption, the activity coefficients of the ions can be considered as unity, and thus the activity of HS^- is constant at 2. By dividing these two equilibrium equations, it can be derived that at dissolution equilibrium, the activity of OH^- should reach 2.5×10^5. This implies that the theoretical concentration of OH^- in the solution should be 2.5×10^5 M. However, such an extremely high concentration is unattainable under practical conditions, meaning the system remains in a state far from equilibrium. Under these conditions, the hydroxides continuously convert into sulfides. This transformation proceeds under mild conditions, preserving the original structure of the hydroxides. During the transformation, both OH^- and S^{2-} coexist in the material, and such a substance is referred to as a hydroxysulfide. In summary, by simply immersing nickel–iron hydroxide in a high-concentration sodium sulfide solution at room temperature, nickel–iron hydroxysulfide (S-NiFe-LDH/NF) can theoretically be obtained.

The morphological evolution of NF, NiFe-LDH/NF, and S-NiFe-LDH/NF was systematically examined using scanning electron microscopy (SEM). As shown in Fig. S2, NF substrate exhibits a three-dimensional macroporous skeleton. After treatment with $Fe(NO_3)_3$ solution, smooth nanosheet-like NiFe-LDH/NF structures uniformly coat the NF framework (Fig. 1a). Notably, following sulfuration at room temperature, the resulting S-NiFe-LDH/NF retains the nanosheet morphology while exhibiting pronounced surface roughening (Fig. 1e). This transformation confirms the successful incorporation of sulfur species without damaging the material's structural integrity.

Transmission electron microscopy (TEM) observations reveal that NiFe-LDH/NF adopts a typical stacked nanosheet architecture. After sulfur doping, its morphology remains largely unchanged, with no apparent structural disruption (Fig. 1b and f). High-resolution TEM (HRTEM) provides

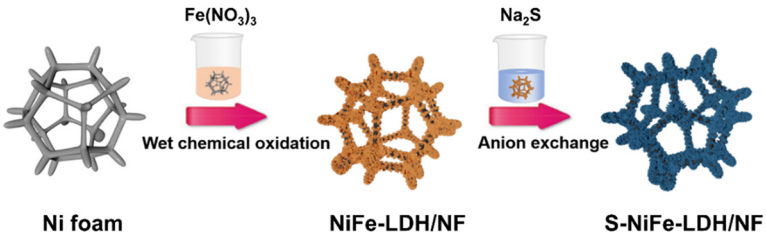

Scheme 1 Schematic illustration of the room-temperature synthesis of S-NiFe-LDH/NF.

Published on 21 January 2026. Downloaded by RSC Internal on 1/28/2026 11:03:34 AM.

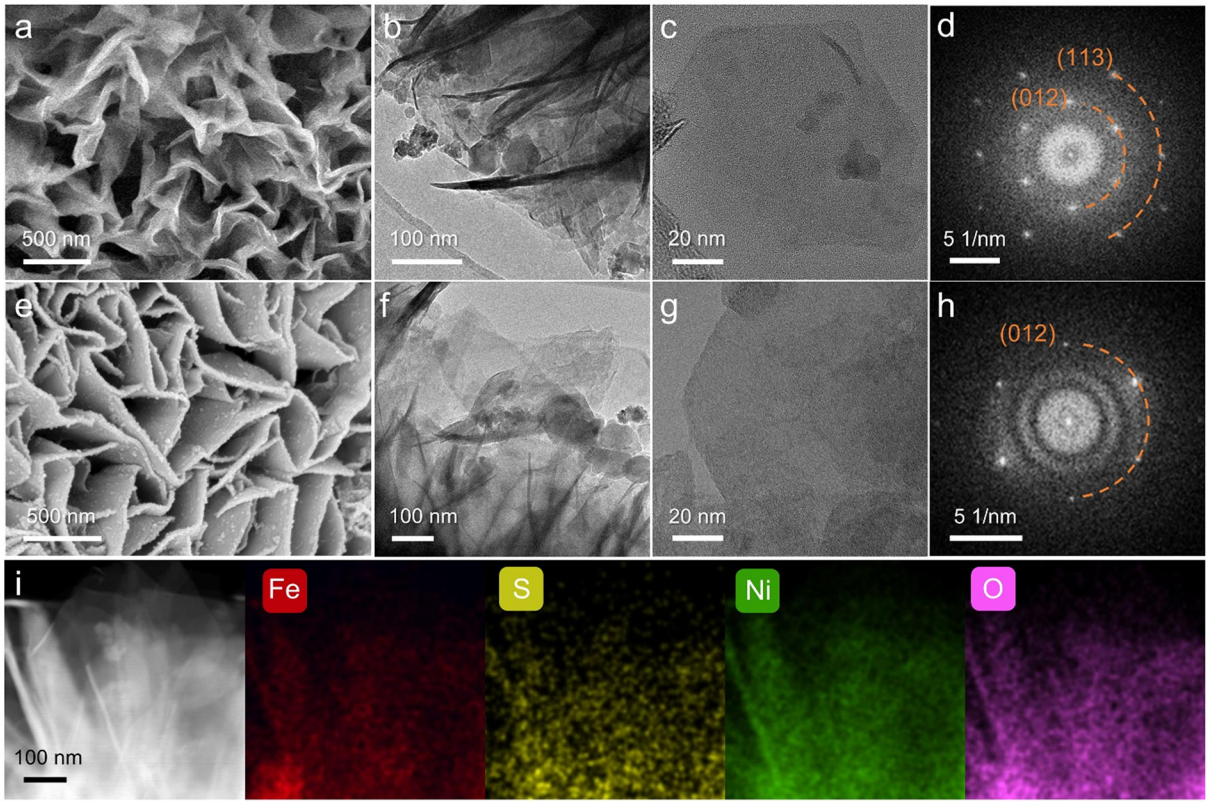

Fig. 1 (a) SEM image, (b) TEM image, (c) HRTEM image, and (d) FFT pattern of the HRTEM image of NiFe-LDH/NF. (e) SEM image, (f) TEM image, (g) HRTEM image, and (h) FFT pattern of the HRTEM image of S-NiFe-LDH/NF. (i) EDS mapping image of S-NiFe-LDH/NF.

further insights into the atomic-scale structure. Both pristine and sulfur-doped NiFe-LDH/NF display well-defined hexagonal symmetry (Fig. 1c and g). The fast Fourier transform (FFT) analysis of the HRTEM image of pristine NiFe-LDH/NF (Fig. 1d) shows clear diffraction spots corresponding to the (1 0 1) plane (d = 0.26 nm) and the (1 1 3) plane (d = 0.15 nm) of LDH. In contrast, while the (1 0 1) plane (d = 0.26 nm) remains discernible in S-NiFe-LDH/NF, the lattice fringes appear significantly blurred, indicating local lattice distortion and reduced crystallinity (Fig. 1h).[41–43]

Furthermore, energy-dispersive X-ray spectroscopy (EDS) elemental mapping confirms the homogeneous distribution of Ni, Fe, O, and S within the nanosheets, providing direct evidence of the uniform incorporation of sulfur into the lattice (Fig. 1i). The resulting S-NiFe-LDH/NF architecture, with its abundant exposed active sites, ultrathin two-dimensional sheet structure, and intimate integration with the highly conductive NF substrate, facilitates efficient electron transport and thus enhances the overall electrocatalytic performance.

The synthesized samples were characterized by X-ray diffraction (XRD) to determine their phase composition and structural features (Fig. 2a). The diffraction peaks at 11.5° and 23.3° correspond to the (0 0 3) and (0 0 6) planes of NiFe-LDH/NF (PDF #51-0463), confirming the successful synthesis of the layered double hydroxide structure. Notably, sulfur doping results in a reduced intensity of XRD peaks, suggesting a decrease in crystallinity. This observation is consistent with the localized lattice distortions revealed in Fig. 1. Furthermore, no characteristic diffraction peaks of Ni_2S_3 (PDF #44-1418) or Ni_3S_4 (PDF #76-1813) were detected in the sulfurized samples.[44,45] This result confirms that the sulfur doping process did not induce phase separation, effectively preserving the structural homogeneity and thereby successfully synthesizing the desired hydroxysulfide. To further verify the compositional features of the material, Fourier-transform infrared (FTIR) spectroscopy analysis shown in Fig. 2b provided essential evidence. The characteristic absorption bands at 1018.23, 1062.58, 1230.84, 1353.78, and 1471.42 cm^{-1} are attributed to the stretching vibrations of S–O, C–O, S═O, $\delta(CO_3^{2-})$, and $\nu(CO_3^{2-})$, respectively, on the surface of S-NiFe-LDH/NF. It is noteworthy that the stretching vibration mode of interlayer CO_3^{2-} exhibited no significant shift, indicating that sulfur species were not intercalated into the interlayer space of NiFe-LDH/NF. The presence of S–O and S═O vibration bands is ascribed to oxidized sulfur species located on the surface of the LDH.[46,47] These multi-scale characterization results effectively confirm that the synthesis pathway illustrated in Scheme 1 successfully enabled the effective incorporation of sulfur into the NiFe-LDH/NF phase, resulting in the target product S-NiFe-LDH/NF.

To further investigate the surface chemical states and compositional variations of NiFe LDH/NF and S-NiFe

This journal is © The Royal Society of Chemistry 2026

Published on 21 January 2026. Downloaded by RSC Internal on 1/28/2026 11:03:34 AM.

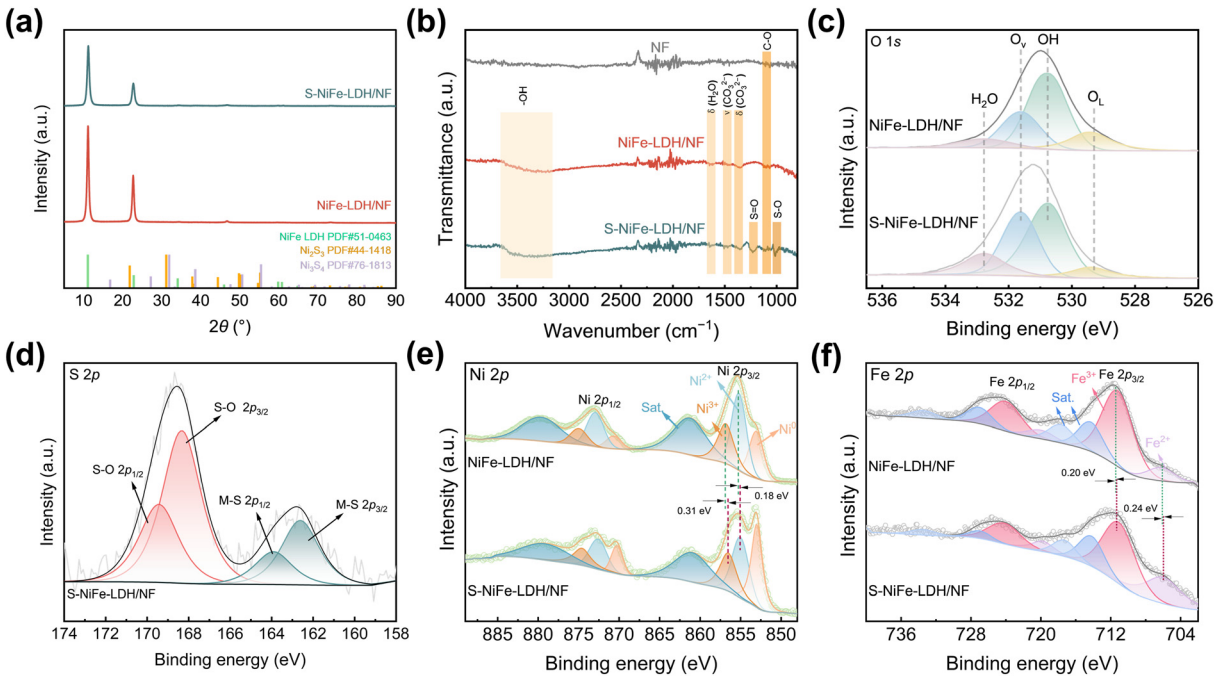

Fig. 2 (a) XRD patterns of NiFe-LDH/NF and S-NiFe-LDH/NF. (b) FTIR spectra of NF, NiFe-LDH/NF and S-NiFe-LDH/NF. (c) XPS spectra of O 1s for NiFe-LDH/NF and S-NiFe-LDH/NF; (d) S 2p XPS spectrum for S-NiFe-LDH/NF; XPS spectra of (e) Ni 2p and (f) Fe 2p for NiFe-LDH/NF and S-NiFe-LDH/NF.

LDH/NF, high-resolution X-ray photoelectron spectroscopy (XPS) was performed. In the O 1s spectra (Fig. 2c), the peaks located at 529.41, 530.75, 531.62, and 532.77 eV correspond to lattice oxygen (O_L), hydroxyl groups (OH), oxygen vacancies (O_V), and adsorbed water (H_2O), respectively.[48] The presence of sulfur in the catalyst before and after doping is confirmed by the S peak observed in the XPS survey spectra (Fig. S5a), and the sulfur content is determined to be 2.98 at.% (Table S1). In the S 2p spectrum (Fig. 2d), the M–S $2p_{1/2}$ (163.91 eV) and M–S $2p_{3/2}$ (162.61 eV) peaks are assigned to metal–sulfur bonds. In addition, two characteristic peaks located at 168.32 eV (S–O $2p_{3/2}$) and 169.42 eV (S–O $2p_{1/2}$) reveal the partial oxidation of sulfur species on the catalyst surface during synthesis.[41]

Since metal sites serve as the true active centres for OER, analysing the electronic structure modulation induced by sulfur doping is of great importance for rational catalyst design. As shown in Fig. 2e, the Ni 2p spectrum of pristine NiFe-LDH/NF displays distinct peaks assigned to metallic Ni^0 (853.05/870.63 eV), Ni^{2+} (855.20/872.76 eV), and Ni^{3+} (856.82/874.55 eV), along with corresponding satellite features at 861.24 and 879.65 eV. Upon sulfur incorporation, the Ni $2p_{3/2}$ peaks for Ni^0, Ni^{2+}, and Ni^{3+} shift toward lower binding energies by 0.05, 0.18, and 0.31 eV, respectively. Similarly, the Fe^{2+} and Fe^{3+} peaks shift negatively by 0.24 and 0.20 eV, respectively (Fig. 2f). The slight decrease in binding energy indicates increased surface electron density of Ni and Fe after S doping, consistent with the lower electronegativity of sulfur. These initially lower-valence metal centers are more readily oxidized under OER conditions, forming a higher density of high-valence active sites.[29] Consequently, sulfur-doped NiFe-LDH/NF is expected to exhibit enhanced OER performance.

3.2. OER catalytic performance

Cyclic voltammetry (CV) was employed to induce surface reconstruction of the NiFe-LDH/NF and S-NiFe-LDH/NF catalysts, ensuring stable and reproducible catalytic performance. The samples treated by 100 cycles of CV activation in 1.0 M KOH electrolyte are designated as R_{100}-NiFe-LDH/NF and R_{100}-S-NiFe-LDH/NF, respectively. Fig. 3a presents the linear sweep voltammetry (LSV) curves of various samples recorded in 1.0 M KOH electrolyte under an argon-saturated atmosphere. To minimize interference from the oxidation peaks of Ni and Fe, a negative scan direction was employed. As shown in Fig. 3b, at a current density of 10 mA cm^{-2}, R_{100}-S-NiFe-LDH/NF exhibits the lowest overpotential of 186 mV compared to R_{100}-NiFe-LDH/NF (187 mV), $Ni(OH)_2$ (222 mV), RuO_2 (301 mV), and NF (343 mV). Notably, at 200 mA cm^{-2}, R_{100}-S-NiFe-LDH/NF still maintains a low overpotential of 235 mV, significantly outperforming the other catalysts (272, 426, 499, and 581 mV, respectively). These results indicate that R_{100}-S-NiFe-LDH/NF exhibits the most favourable OER activity among the tested materials. The structural defects and electronic state changes induced by surface reconstruction, which underpin this superior performance, will be further discussed in the subsequent mechanistic analysis section.

Published on 21 January 2026. Downloaded by RSC Internal on 1/28/2026 11:03:34 AM.

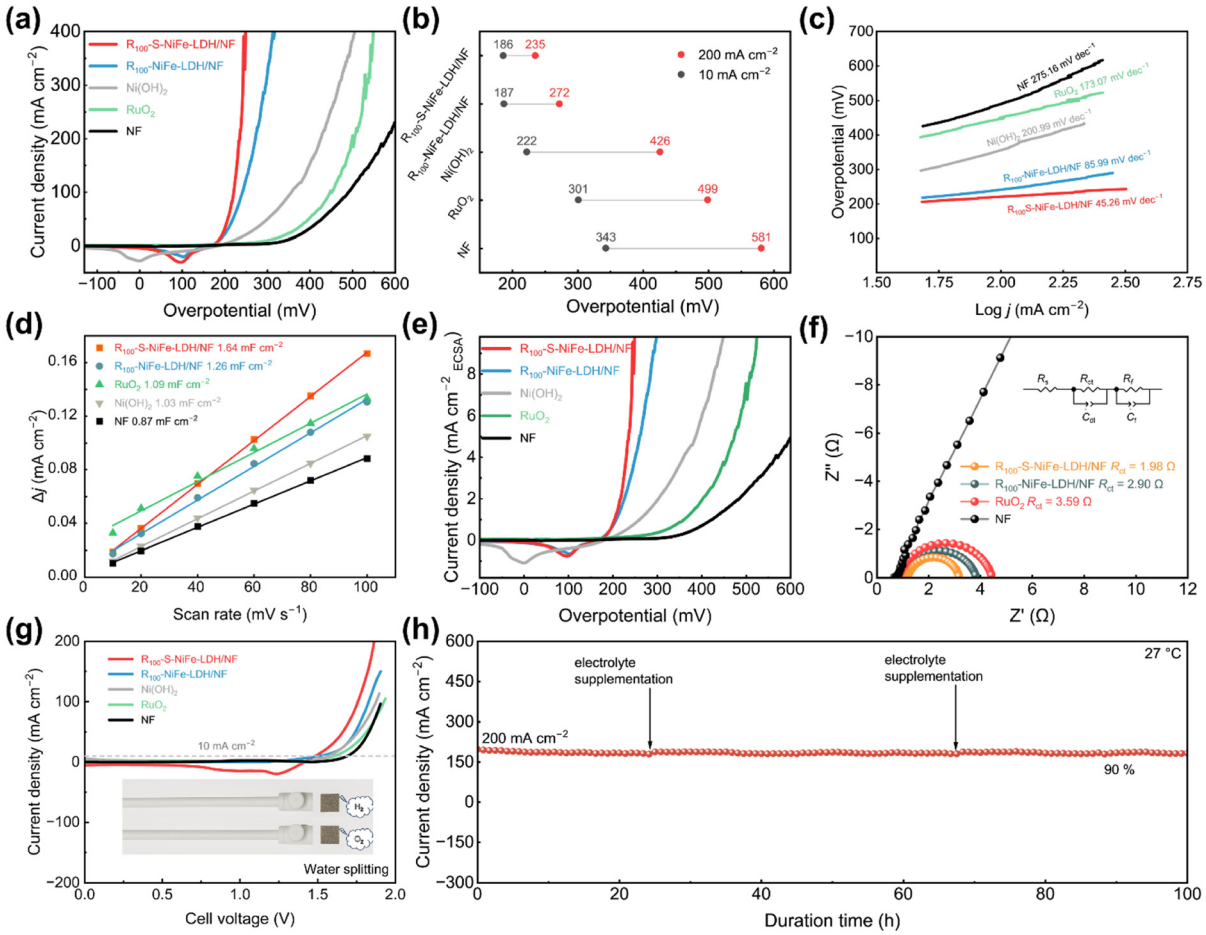

Fig. 3 Electrochemical performance of R_{100}-NiFe-LDH/NF, R_{100}-S-NiFe-LDH/NF, $Ni(OH)_2$, RuO_2 and NF in 1.0 M KOH. (a) LSV curves with 95% iR compensation for the different catalysts; (b) comparison of overpotentials at 10 mA cm^{-2} and 200 mA cm^{-2}; (c) Tafel slope plot; (d) plot of capacitive current *versus* scan rate, with the C_{dl} determined by linear fitting; (e) LSV curves of different catalysts, normalized by electrochemically active surface area (ECSA) for current density; (f) Nyquist plot of the electrochemical impedance test before and after 100 cycles of CV for the catalyst; equivalent circuit diagram used for fitting the electrochemical impedance data (R_s represents the electrolyte resistance, C_{dl} represents the double-layer capacitance, R_{ct} represents the charge transfer resistance, R_f represents the catalyst resistance, C_f represents the catalyst capacitance); (g) LSV curves for overall water splitting in 1 M KOH. (h) *i*–*t* curve of R_{100}S-NiFe-LDH/NF at an initial current density of 200 mA cm^{-2}.

The corresponding Tafel plots derived from the LSV data are shown in Fig. 3c. The Tafel slopes for R_{100}-S-NiFe-LDH/NF, R_{100}-NiFe-LDH/NF, $Ni(OH)_2$, RuO_2, and NF are 45.26, 85.99, 200.99, 173.07, and 275.16 mV dec^{-1}, respectively. The significantly lower Tafel slope of R_{100}-S-NiFe-LDH/NF implies more favourable reaction kinetics and a faster OER process. Tafel slopes also offer mechanistic insights into the rate-determining step (RDS) of the OER.[49,50] The OER process typically proceeds *via* the following four elementary steps:

$OH^- + * \rightarrow OH^* + e^-$	Step 1
$OH^* + OH^- \rightarrow O^* + H_2O + e^-$	Step 2
$O^* + OH^- \rightarrow OOH^* + e^-$	Step 3
$OOH^* + OH^- \rightarrow O_2 + H_2O + e^- + *$	Step 4

Theoretical Tafel slopes corresponding to these steps are ~120, ~60, and ~40 mV dec^{-1} for steps 1 to 3, respectively. The observed Tafel slope of 45.26 mV dec^{-1} for R_{100}-S-NiFe-LDH/NF suggests that the third step, namely the formation of the OOH* intermediate. In contrast, the RDS for R_{100}-NiFe-LDH/NF is attributed to the second step involving O* formation. This result indicates that sulfur incorporation not only enhances catalytic activity but also alters the intrinsic OER reaction pathway.[51]

The electrochemical surface area (ECSA) is a critical parameter for evaluating catalytic activity and can be estimated by measuring the double-layer capacitance (C_{dl}), which is linearly correlated with ECSA.[52] As shown in Fig. 3d and Fig. S3, the C_{dl} values for R_{100}-S-NiFe-LDH/NF, R_{100}-NiFe-LDH/NF, $Ni(OH)_2$, RuO_2, and NF are 1.64, 1.26, 1.03, 1.09, and 0.87 mF cm^{-2}, respectively. Based on section 2.3, the ECSA of R_{100}-S-NiFe-LDH/NF is calculated to be 41.0 cm^2, which is 1.3 and 1.6 times greater than that of R_{100}-NiFe-LDH/NF (31.5 cm^2) and $Ni(OH)_2$ (25.75 cm^2), respectively. After normalizing the LSV curves to ECSA (Fig. 3e), it is evident that R_{100}-S-NiFe-LDH/NF still exhibits superior intrinsic OER activity. This result indicates that sulfur doping effectively enhances the surface reconstruction of NiFe-LDH/

This journal is © The Royal Society of Chemistry 2026

Published on 21 January 2026. Downloaded by RSC Internal on 1/28/2026 11:03:34 AM.

NF, leading to increased electrochemical surface exposure and a greater density of active sites. Electrochemical impedance spectroscopy (EIS) was conducted to probe the interfacial charge transport behaviour.[53] The Nyquist plots recorded at 1.5 V (*vs.* RHE) are displayed in Fig. 3f. The charge transfer resistance (R_{ct}), extracted by fitting the data using an equivalent circuit model, serves as a key indicator of electron-transfer kinetics. After 100 cycles of CV activation, both NiFe-LDH/NF and S-NiFe-LDH/NF exhibit reduced R_{ct} values, with R_{100}-S-NiFe-LDH/NF showing the lowest resistance of 1.98 Ω. This finding suggests that sulfur incorporation facilitates the generation of conductive active phases and improves interfacial electron transport.[54] In contrast, the bare NF substrate exhibits a much higher R_{ct}, indicating its limited contribution to the catalytic process apart from electrical conductivity.

A two-electrode electrolyser was assembled with the catalysts as both anode and cathode to assess their overall water splitting performance in 1 M KOH (Fig. 3g). As shown in the results, the R_{100}-S-NiFe-LDH/NF-based device required only 1.49 V to reach a current density of 10 mA cm^{-2}, outperforming its counterparts: R_{100}-NiFe-LDH/NF (1.51 V), $Ni(OH)_2$ (1.57 V), commercial RuO_2 (1.61 V), and bare NF (1.69 V). These findings highlight the potential of the R_{100}-S-NiFe-LDH/NF catalyst in water electrolysis for hydrogen production.

Catalyst stability is also a critical parameter for evaluating overall performance. As shown in Fig. 3h, the R_{100}-S-NiFe-LDH/NF catalyst was subjected to a long-term electrolysis test in 1.0 M KOH at an initial current density of 200 mA cm^{-2}. After 100 hours of continuous operation, it retained more than 90% of its initial current, demonstrating excellent structural integrity and electrochemical durability. In addition, the stability test of pristine NiFe-LDH/NF (Fig. S4) shows that its current retention is only 82.6% under the same conditions. This comparison clearly indicates that sulfur incorporation improves the long-term stability from 82.6% to approximately 90%.

3.3. Catalytic mechanism analysis

In oxygen evolution reaction systems, surface reconstruction can significantly influence the catalytic activity and selectivity, thereby affecting both reaction efficiency and product distribution.[55,56] During the reconstruction process, surface atomic layers may undergo rearrangement, leading to the formation of new crystal structures or surface phases. The specific mechanism and dynamic evolution of surface reconstruction are synergistically regulated by multiple factors, including the catalyst composition, microstructural characteristics, and reaction environment. Herein, a detailed analysis of the aforementioned CV activation of the catalysts is presented to elucidate their reconstruction behavior.

As shown in Fig. 4a and b, the comparison of CV curves reveals that, upon continuous cycling, the intensity of the Ni^{2+}/Ni^{3+} redox peaks progressively increases and eventually

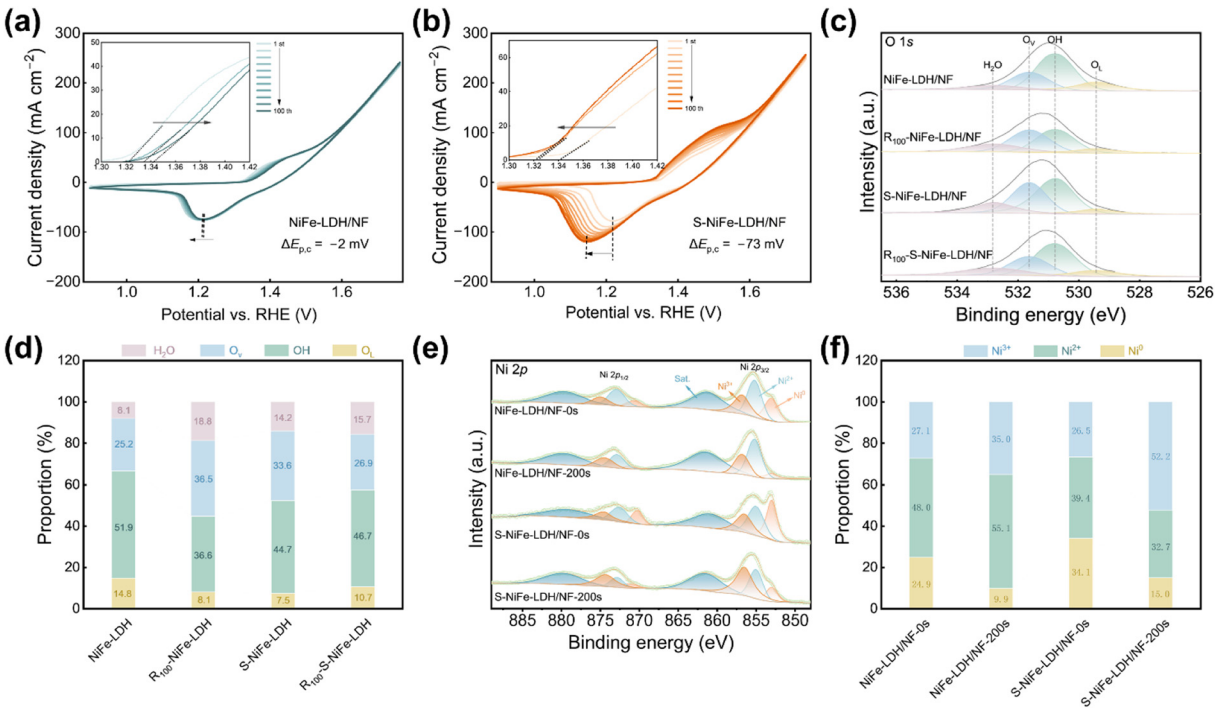

Fig. 4 CV reconstruction plots of the catalysts: (a) S-NiFe-LDH/NF and (b) NiFe-LDH/NF. The insets show enlarged LSV curves in the potential range of 1.30–1.42 V with the same axis labels as the main plots. (c) O 1s XPS spectra of the catalysts before and after 100 cycles of CV; (d) percentage composition of lattice oxygen (O_L), hydroxyl (OH), oxygen vacancies (O_V) and adsorbed water (H_2O). (e) Ni 2p XPS spectra before and after 200 seconds of catalyst reaction; (f) percentage content map of Ni^0, Ni^{2+}, and Ni^{3+}.

Published on 21 January 2026. Downloaded by RSC Internal on 1/28/2026 11:03:34 AM.

stabilizes. This redox couple is represented by a pair of peaks, including a pronounced anodic shoulder and a distinct cathodic dip visible as a downward valley during the reverse scan. The enlarged area of this redox feature suggests the generation of new surface-active sites. Compared with R_{100}-NiFe-LDH/NF, the sulfur-doped R_{100}-S-NiFe-LDH/NF exhibits a lower onset potential for nickel oxidation (1.32 V *vs.* RHE) and a more significant cathodic shift ($\Delta E_{p,c}$ = −73 mV), indicating the accelerated formation of active species due to sulfur incorporation. Additionally, its higher redox peak current density reflects an intensified surface reconstruction process facilitated by sulfur modulation.[29]

As shown in the XPS O 1s spectra in Fig. 4c and the quantified proportions of oxygen species in Fig. 4d, changes in the relative content of different oxygen species reveal distinct surface evolution behaviours. For NiFe-LDH/NF, after 100 cycles of CV testing, the proportion of oxygen vacancies (O_V) increases from 25.2% to 36.5%, while the proportion of lattice oxygen (O_L) decreases from 14.8% to 8.1%. This loss of O_L is likely due to lattice oxygen participation in the OER *via* the lattice oxygen mechanism (LOM). In contrast, the S-NiFe-LDH/NF exhibits the opposite trend: the O_V content decreases from 33.6% to 26.9%, and the O_L content increases from 7.5% to 10.7%. This indicates that sulfur doping effectively suppresses the escape of lattice oxygen and inhibits the formation of oxygen vacancies, thereby contributing to the preservation of the catalyst's surface structural integrity during the OER process.[57] Importantly, the S 2p signal remains clearly observable in the full XPS survey spectra even after 100 CV cycles (Fig. S5b), confirming the sustained presence of sulfur species throughout the electrochemical activation process.

As shown in the Ni 2p spectra (Fig. 4e), the evolution of nickel valence states was investigated after a 200-second OER test at a current density of 10 mA cm^{-2}. Compared to NiFe-LDH/NF, the S-NiFe-LDH/NF sample displayed a markedly higher proportion of high-valence Ni species on the surface (Fig. 4f). To further quantify this change, the $Ni^{3+}/(Ni^{2+} + Ni^{3+})$ ratio was determined from the deconvoluted Ni 2p XPS spectra. For NiFe-LDH/NF, the ratio slightly increased from 36.1% to 38.8% after OER, whereas a more pronounced rise from 40.2% to 61.4% was observed for S-NiFe-LDH/NF. This enhanced enrichment of Ni^{3+} species under identical conditions indicates that sulfur incorporation facilitates the oxidation of low-valence nickel into catalytically active Ni^{3+} during the OER process.[51,58] Moreover, the higher Ni^{3+} content suggests improved redox robustness of nickel sites under operating conditions.

Finally, steady-state polarization curves of NiFe-LDH/NF and S-NiFe-LDH/NF were recorded under pH conditions ranging from 12 to 14 to elucidate the differences in their OER reaction pathways (Fig. S6a–b). As the pH increased, both catalysts exhibited elevated current densities at the same overpotential, showing a clear pH dependence. Such behaviour is typically associated with the lattice-oxygen-mediated mechanism (LOM), suggesting that a certain degree of lattice oxygen participation may occur during the OER process.[59] To quantitatively assess this pH sensitivity, we calculated the proton reaction order ρ on the RHE scale ($\rho^{RHE} = \partial \log j / \partial pH$). The results reveal that the ρ value of the undoped sample is 0.94, whereas *S* doping lowers this value to approximately 0.77 (Fig. S6c). Considering that the classical adsorbate evolution mechanism (AEM) generally exhibits a pH-independent rate ($\rho^{RHE} \approx 0$), the reduced reaction order after *S* incorporation indicates a weakened involvement of lattice oxygen, implying a partial suppression of LOM behaviour.[60] In summary, the pH-dependent measurements demonstrate that the *S* doping in NiFe-LDH reduces lattice oxygen participation and modulates the reaction pathway of OER, thereby mitigating structural instability caused by excessive oxidation and enhancing the overall reaction stability.

In summary, sulfur doping in S-NiFe-LDH/NF not only suppresses the formation of oxygen vacancies (O_V) and inhibits the loss of lattice oxygen (O_L), thereby preserving lattice integrity, but also significantly stabilizes the catalytically active high-valence Ni species. Additionally, the reduced pH dependence of the OER current indicates that sulfur doping suppresses lattice-oxygen participation in the reaction. These findings strongly support that the incorporation of sulfur mitigates the LOM pathway by reinforcing structural robustness, effectively preventing the deactivation or transformation of Ni^{3+} species caused by structural degradation during the OER. As a result, the catalyst exhibits enhanced structural stability and active site durability under long-term OER operation.

4. Conclusions

In this study, sulfur-doped NiFe-LDH/NF nanosheets were successfully constructed on nickel foam (NF) substrates *via* a simple two-step room-temperature immersion method, followed by electrochemical reconstruction through CV cycling, yielding a high-performance OER catalyst (R_{100}-S-NiFe-LDH/NF). The catalyst exhibited excellent performance in 1 M KOH, characterized by a low overpotential of 186 mV at 10 mA cm^{-2} and 235 mV at 200 mA cm^{-2}, along with a small Tafel slope of 45.26 mV dec^{-1}. Its electrochemical surface area increased to 1.3 times that of the undoped counterpart, indicating a greater exposure of active sites. Remarkably, R_{100}-S-NiFe-LDH/NF maintained stable operation for over 100 hours at an industrial-level current density of 200 mA cm^{-2}, with only a 10% performance loss, highlighting its strong potential for commercial application. Mechanistic investigations revealed that sulfur doping enhances catalytic performance through a dual-pathway mechanism: on one hand, *S*-mediated electronic modulation significantly increases the valence states of Ni and Fe, while simultaneously suppressing lattice oxygen loss and oxygen vacancy formation, thereby preserving structural stability; on the other hand, sulfur alters the surface reconstruction kinetics of NiFe-LDH/NF, promoting the

This journal is © The Royal Society of Chemistry 2026

Published on 21 January 2026. Downloaded by RSC Internal on 1/28/2026 11:03:34 AM.

exposure of additional active sites during reconstruction, which further boosts OER activity. This green strategy, combining room-temperature synthesis with electrochemical reconstruction, offers a promising and cost-effective approach for the development of efficient OER electrocatalysts.

Author contributions

Pei-Wei Zhong: validation, data curation, writing (original draft) and writing (review & editing). Hong-Xiao Yang: investigation, data curation and methodology. Wenkang Xu: data curation and formal analysis. Zhiyang Yu: data curation and formal analysis. Bei Li: data curation and formal analysis. Yuguang Jin: resources. Hongjuan Wang: supervision and writing (review & editing). Yonghai Cao: supervision and writing (review & editing). Hao-Fan Wang: funding acquisition, project administration, supervision and writing (review & editing). Yanhui Yang: supervision and resources. Hao Yu: funding acquisition, project administration, supervision and writing (review & editing).

Conflicts of interest

The authors declare no competing interests.

Data availability

The data supporting this article have been included as part of the supplementary information (SI). Supplementary information is available. See DOI: https://doi.org/10.1039/d5re00397k.

Acknowledgements

This work is financially supported by National Natural Science Foundation of China (No. 22209049) and Natural Science Foundation of Guangdong Province (No. 2023A1515012804, 2024B1515040016, 2025A1515010003).

References

1 P. Pazhamalai, K. Krishnamoorthy, R. Swaminathan, V. Natraj and S. J. Kim, *Nano Energy*, 2024, **120**, 109084.
2 M. Vanags, G. Kulikovskis, J. Kostjukovs, L. Jekabsons, A. Sarakovskis, K. Smits, L. Bikse and A. Sutka, *Energy Environ. Sci.*, 2022, **15**, 2021–2028.
3 H. F. Wang, C. Tang and Q. Zhang, *J. Mater. Chem. A*, 2015, **3**, 16183–16189.
4 H. F. Wang and Q. Xu, *Matter*, 2019, **1**, 565–595.
5 H. J. W. Li, Y. Lin, J. Y. Duan, Q. L. Wen, Y. W. Liu and T. Y. Zhai, *Chem. Soc. Rev.*, 2024, **53**, 10709–10740.
6 P. Trivedi, N. C. Minj, S. Mittal, B. Kamaraj, S. Yadav and A. Sengeni, *J. Mater. Chem. A*, 2025, **13**, 21436–21452.
7 H. F. Wang, C. Tang, B. Q. Li and Q. Zhang, *Inorg. Chem. Front.*, 2018, **5**, 521–534.
8 H. X. Yang, W. K. Xu, P. W. Zhong, D. L. Zhang, Z. Y. Yu, B. Li, H. J. Wang, Y. H. Cao, H. F. Wang and H. Yu, *J. Energy Chem.*, 2025, **105**, 121–129.
9 H. J. Zhang, Z. Q. Chen, X. T. Ye, K. Xiao and Z. Q. Liu, *Angew. Chem., Int. Ed.*, 2025, **64**, e202421027.
10 Z. Q. Ge, J. W. Li, H. J. Zhang, C. B. Liu, G. B. Che and Z. Q. Liu, *Adv. Funct. Mater.*, 2024, **34**, 2411024.
11 J. X. Chen, Q. W. Long, K. Xiao, T. Ouyang, N. Li, S. Y. Ye and Z. Q. Liu, *Sci. Bull.*, 2021, **66**, 1063–1072.
12 K. Saito, M. Morita, T. Okada, R. Wijitwongwan and M. Ogawa, *Chem. Soc. Rev.*, 2024, **53**, 10523–10574.
13 C. Tang, H. F. Wang, X. L. Zhu, B. Q. Li and Q. Zhang, *Part. Part. Syst. Charact.*, 2016, **33**, 473–486.
14 M. Mehdi, B. S. An, H. Kim, S. Lee, C. Lee, M. Seo, M. W. Noh, W. C. Cho, C. H. Kim, C. H. Choi, B. H. Kim, M. Kim and H. S. Cho, *Adv. Energy Mater.*, 2023, **13**, 2204403.
15 Y. Y. Zhai, X. R. Ren, Y. Sun, D. Li, B. L. Wang and S. Liu, *Appl. Catal., B*, 2023, **323**, 122091.
16 X. M. Liu, X. Fan, H. Huang, H. P. Lin and J. Z. Gao, *J. Colloid Interface Sci.*, 2021, **587**, 385–392.
17 X. Lyu, Y. Zhang, X. Wang, H. Chen, S. Li, W. Zhang, Y. Hu, F. Li, D. Li and D. Yang, *Mater. Today Sustain.*, 2023, **21**, 100295.
18 F. Huang, W. L. Liang, H. X. Yang, Y. Q. Dai, H. J. Wang, Y. H. Cao, H. Yu and H. F. Wang, *Adv. Sustainable Syst.*, 2025, **9**, e00457.
19 L. T. Wei, M. Y. Du, R. Zhao, F. Lv, L. B. Li, L. Zhang, D. Zhou and J. Z. Su, *J. Mater. Chem. A*, 2022, **10**, 23790–23798.
20 B. Wang, J. W. Chen, L. Luo, G. K. Huang, Q. Shi, Q. L. Wei, M. H. Shang and Q. Liu, *Adv. Funct. Mater.*, 2025, **35**, 2505763.
21 Y. J. Li, Y. P. Liu, Y. C. Chen, T. Liu, X. Y. Liu, S. J. Ni, J. Ru, F. B. Meng, M. Li and Z. Q. Cao, *J. Mater. Chem. A*, 2025, **13**, 12374–12382.
22 L. Naderi and S. Shahrokhian, *Nanoscale*, 2024, **16**, 20260–20279.
23 H. Lei, Q. X. Wan, S. Z. Tan, Z. L. Wang and W. J. Mai, *Adv. Mater.*, 2023, **35**, 2208209.
24 S. S. Roy, R. K. Sharma, A. Karmakar, S. Nagappan, B. Pathak and S. Kundu, *Appl. Catal., B*, 2025, **371**, 125227.
25 J. T. Zhang, Y. Yang, G. X. Ding, Z. Q. Wang, P. Wang, C. N. X. Li and G. F. Liao, *Chem. Eng. J.*, 2025, **505**, 159165.
26 T. Susikumar, P. J. Jesuraj, M. Navaneethan, A. D. Savariraj, C. M. Lee and S. Y. Ryu, *Surf. Interfaces*, 2024, **55**, 105448.
27 B. Zheng, Y. Chen, S. Q. Ding, Y. Zhou, Z. R. Pan, Y. J. Hu, W. S. Chen, X. F. Wang, G. X. Liu and L. M. Lang, *Int. J. Hydrogen Energy*, 2024, **51**, 681–687.
28 Y. Q. Yang, S. L. Ma, M. Q. Xia, Y. Guo, Y. Zhang, L. W. Liu, C. Zhou, G. H. Chen, X. Z. Wang, Q. Wu, L. J. Yang and Z. Hu, *Mater. Today Phys.*, 2023, **35**, 101112.
29 H. Lei, L. Ma, Q. X. Wan, S. Z. Tan, B. Yang, Z. L. Wang, W. J. Mai and H. J. Fan, *Adv. Energy Mater.*, 2022, **12**, 2202522.
30 Q. H. Su, P. Y. Wang, Q. C. Liu, R. Sheng, W. H. Cheng, J. Ding, Y. P. Lei and Y. D. Huang, *Appl. Catal., B*, 2024, **351**, 123994.
31 X. G. Li, J. Zhao, J. H. Zhou, Q. C. Wang and J. Han, *Green Chem.*, 2023, **25**, 10684–10692.
32 K. R. Kumar, N. D. Sri, V. N. Kale and T. Maiyalagan, *Int. J. Hydrogen Energy*, 2025, **101**, 837–847.

Published on 21 January 2026. Downloaded by RSC Internal on 1/28/2026 11:03:34 AM.

33 Z. Q. Chen, W. J. Cai, H. J. Zhang, K. Xiao, B. L. Huang and Z. Q. Liu, *Chem. Sci.*, 2025, **16**, 14750–14759.
34 H. X. Liao, G. H. Ni, P. F. Tan, Y. Liu, K. J. Chen, G. M. Wang, M. Liu and J. Pan, *Appl. Catal., B*, 2022, **317**, 121713.
35 K. Jiang, Q. Li, S. F. Lei, M. D. Zhai, M. Cheng, L. Xu, Y. L. Deng, H. Xu and J. Bao, *Electrochim. Acta*, 2022, **429**, 140947.
36 H. F. Wang, C. Tang, B. Wang, B. Q. Li and Q. Zhang, *Adv. Mater.*, 2017, **29**, 1702327.
37 B. Wang, C. Tang, H. F. Wang, X. Chen, R. Cao and Q. Zhang, *J. Energy Chem.*, 2019, **38**, 8–14.
38 C. M. Flynn, Jr., *Chem. Rev.*, 1984, **84**, 31–41.
39 Y. J. Wu, J. Yang, T. X. Tu, W. Q. Li, P. F. Zhang, Y. Zhou, J. F. Li, J. T. Li and S. G. Sun, *Angew. Chem., Int. Ed.*, 2021, **60**, 26829–26836.
40 A. Hai, M. Daud, G. Mujtaba, F. Banat and M. A. Al-Harthi, *Coord. Chem. Rev.*, 2025, **529**, 216435.
41 Y. Ge, Y. Wang, Z. F. Liu, X. B. Xu, Y. Q. Chen, Z. L. Yin, Q. Zhou and W. B. Yang, *Water Res.*, 2025, **274**, 123077.
42 D. H. Xie, W. Q. Li, N. Xu, L. Yuan, W. H. Zhang, T. Y. Huang and G. P. Sheng, *Water Res.*, 2024, **257**, 121695.
43 Y. M. Zhu, J. A. Wang, G. Weiser, M. Klingenhof, T. Koketsu, S. H. Liu, Y. C. Pi, G. Henkelman, X. Y. Shi, J. Y. Li, C. W. Pao, M. H. Yeh, W. H. Huang, P. Strasser and J. W. Ma, *Adv. Energy Mater.*, 2025, **15**, 2500554.
44 C. G. Kuai, Z. R. Xu, C. Xi, A. Y. Hu, Z. J. Yang, Y. Zhang, C. J. Sun, L. X. Li, D. Sokaras, C. K. Dong, S. Z. Qiao, X. W. Du and F. Lin, *Nat. Catal.*, 2020, **3**, 743–753.
45 S. J. Liu, B. R. Jia, Y. Wang, Y. Z. Zhao, L. Liu, F. S. Fan, Y. P. Qin, J. F. Liu, Y. R. Jiang, H. R. Liu, H. Zhao, H. Li, W. X. Zhou, H. Y. Wu, D. Y. Zhang, X. H. Qu and M. L. Qin, *Adv. Mater.*, 2024, **36**, 2409530.
46 W. C. Cheng, H. P. Tang, T. Kai, R. X. Zhao, J. F. Wang and C. C. Ding, *J. Hazard. Mater.*, 2022, **437**, 129352.
47 D. N. Li, M. U. Mushtaq, Y. M. Tang, S. Li, F. B. Hou, K. S. Ayub, L. M. Cao and J. Yang, *Res. Chem. Intermed.*, 2025, **51**, 3019–3038.
48 Q. Zhang, W. Xiao, H. C. Fu, X. L. Li, J. L. Lei, H. Q. Luo and N. B. Li, *ACS Catal.*, 2023, **13**, 14975–14986.
49 X. Q. Gao, Y. T. Chen, Y. J. Wang, L. Y. Zhao, X. Y. Zhao, J. Du, H. X. Wu and A. B. Chen, *Nano-Micro Lett.*, 2024, **16**, 237.
50 J. M. van der Zalm, J. Quintal, S. A. Hira, S. Chen and A. C. Chen, *Electrochim. Acta*, 2023, **439**, 141715.
51 Z. H. Wan, Z. Z. Ma, H. F. Yuan, K. Liu and X. G. Wang, *ACS Appl. Energy Mater.*, 2022, **5**, 4603–4612.
52 S. S. Jeon, P. W. Kang, M. Klingenhof, H. Y. J. Lee, F. Dionigi and P. Strasser, *ACS Catal.*, 2023, **13**, 1186–1196.
53 B. A. Mei, J. Lau, T. Lin, S. H. Tolbert, B. S. Dunn and L. Pilon, *J. Phys. Chem. C*, 2018, **122**, 24499–24511.
54 L. Y. Wang, L. Lin, H. X. Zhang, J. Yu and L. J. Chen, *Mater. Lett.*, 2024, **365**, 136429.
55 Z. Lu, J. K. Wang, P. F. Zhang, W. H. Guo, Y. Q. Shen, P. Z. Liu, J. L. Ji, H. Y. Du, M. Zhao, H. J. Liang and J. J. Guo, *Appl. Catal., B*, 2024, **353**, 124073.
56 H. S. Hu, X. L. Wang, Z. R. Zhang, J. H. Liu, X. H. Yan, X. L. Wang, J. C. Wang, J. P. Attfield and M. H. Yang, *Adv. Mater.*, 2025, **37**, 2415421.
57 J. X. Long, J. H. Zhang, L. F. Li, Y. X. Wen, X. T. Xu and F. Wang, *Int. J. Hydrogen Energy*, 2024, **90**, 1424–1434.
58 P. Wang, L. P. Hao, H. X. Wang and X. W. Liu, *J. Electroanal. Chem.*, 2023, **947**, 117788.
59 F. Q. Wang, P. C. Zou, Y. Y. Zhang, W. L. Pan, Y. Li, L. M. Liang, C. Chen, H. Liu and S. J. Zheng, *Nat. Commun.*, 2023, **14**, 6019.
60 C. Wang, P. L. Zhai, M. Y. Xia, Y. Z. Wu, B. Zhang, Z. W. Li, L. Ran, J. F. Gao, X. M. Zhang, Z. Z. Fan, L. C. Sun and J. G. Hou, *Angew. Chem., Int. Ed.*, 2021, **60**, 27126–27134.

 This journal is © The Royal Society of Chemistry 2026